

AD-A175 153

A MAXIMUM-ENTROPY TECHNIQUE FOR DECONVOLUTION OF
ATMOSPHERIC BREMSSTRAHLU (U) AEROSPACE CORP EL SEGUNDO
CA SPACE SCIENCES LAB D J GORNEY ET AL 15 OCT 86

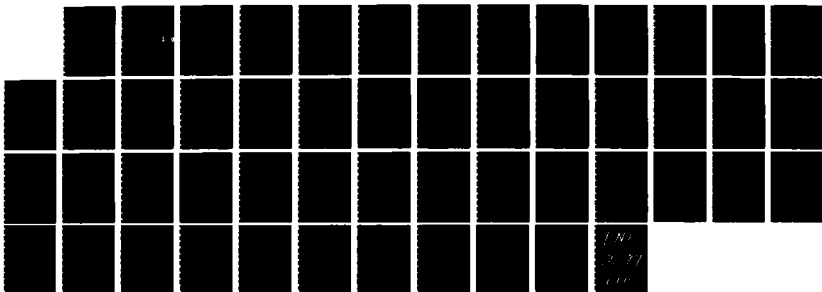
171

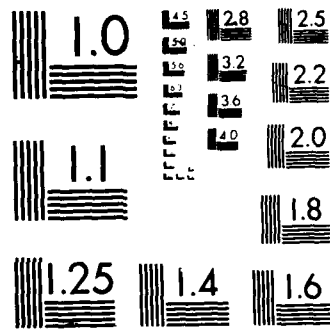
UNCLASSIFIED

TR-8886A(2948-86)-1 SD-TR-86-65

F/G 4/1

NL





PHOTOCOPY RESOLUTION TEST CHART

12

AD-A175 153

A Maximum-Entropy Technique for Deconvolution of Atmospheric Bremsstrahlung Spectra

D. J. GORNEY, P. F. MIZERA, and J. L. ROEDER
Space Sciences Laboratory
Laboratory Operations
The Aerospace Corporation
El Segundo, CA 90245

15 October 1986

DTIC
ELECTE
DEC 18 1986
S D

Prepared for
SPACE DIVISION
AIR FORCE SYSTEMS COMMAND
Los Angeles Air Force Station
P.O. Box 92960, Worldway Postal Center
Los Angeles, CA 90009-2960

DTIC FILE COPY

APPROVED FOR PUBLIC RELEASE:
DISTRIBUTION UNLIMITED

86 12 17 015

This report was submitted by The Aerospace Corporation, El Segundo, CA 90245, under Contract No. F04701-85-C-0086-P00016 with the Space Division, P.O. Box 92960, Worldway Postal Center, Los Angeles, CA 90009-2960. It was reviewed and approved for The Aerospace Corporation by H. R. Rugge, Director, Space Sciences Laboratory.

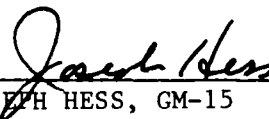
Capt Douglas R. Case/YCM was the project officer for the Mission-Oriented Investigation and Experimentation (MOIE) Program.

This report has been reviewed by the Public Affairs Office (PAS) and is releasable to the National Technical Information Service (NTIS). At NTIS, it will be available to the general public, including foreign nationals.

This technical report has been reviewed and is approved for publication. Publication of this report does not constitute Air Force approval of the report's findings or conclusions. It is published only for the exchange and stimulation of ideas.



DOUGLAS R. CASE, Capt, USAF
MOIE Project Officer
SD/YCM



JOSEPH HESS, GM-15
Director, AFSTC West Coast Office
AFSTC/WCO OL-AB

SECURITY CLASSIFICATION OF THIS PAGE (When Data Entered)

00 FORM 1473
FACSIMILE

SECURITY CLASSIFICATION OF THIS PAGE (When Data Entered)

UNCLASSIFIED

SECURITY CLASSIFICATION OF THIS PAGE(When Data Entered)

19. KEY WORDS (Continued)

20. ABSTRACT (Continued)

provides a statistically optimal estimator of a continuous quantity (in this case, the electron spectrum) when a discrete set of integral functions of that quantity are known (namely, the observed X-ray spectrum). A numerical maximum-entropy deconvolution scheme has been developed and applied to bremsstrahlung X-ray measurements from the Aerospace X-ray spectrometer on DMSP-F6. Good results have been obtained for inferred electron spectra acquired from a variety of auroral forms. These results are presented, and the stability and uniqueness of the solutions are discussed.

UNCLASSIFIED

SECURITY CLASSIFICATION OF THIS PAGE(When Data Entered)

CONTENTS

I.	INTRODUCTION.....	7
II.	BREMSSTRAHLUNG PRODUCTION.....	9
III.	MAXIMUM ENTROPY DECONVOLUTION.....	21
IV.	EXAMPLES.....	25
V.	SUMMARY.....	41
	REFERENCES.....	43
	APPENDIX.....	45

Accession For	
NTIS CRA&I	<input checked="" type="checkbox"/>
DIIC TAB	<input type="checkbox"/>
Unannounced	<input type="checkbox"/>
Justification	
By	
Distribution /	
Availability Codes	
Dist	Avail and/or Special
A-1	



FIGURES

1.	Plot Exhibiting the Plane-Parallel Geometry Used in All Computations in This Report.....	10
2.	Plot of the Bethe-Heitler Cross Section for an Air Target.....	13
3.	Plot of the Bremsstrahlung Production at Energy K of Unit Incident Electron Flux at Energy T for a Geometric Progression of Energy Channels.....	19
4a.	Plots of Input and Inferred Electron Spectra for 1 keV Maxwellian.....	26
4b.	Plots of Input and Inferred Electron Spectra for 10 keV Maxwellian.....	27
4c.	Plots of Input and Inferred Electron Spectra for 5 keV Maxwellian with a 10 keV $\sigma = 2$ Gaussian Peak.....	28
5a.	Plots of Input and Inferred Electron Spectra Incorporating a Simulated Instrumented Response to the Observed X-Ray Spectra for 1 keV Maxwellian.....	30
5b.	Plots of Input and Inferred Electron Spectra Incorporating a Simulated Instrument Response to the Observed X-Ray Spectra for 10 keV Maxwellian.....	31
5c.	Plots of Input and Inferred Electron Spectra Incorporating a Simulated Instrument Response to the Observed X-Ray Spectra for 5 keV Maxwellian with a 10 keV $\sigma = 2$ Gaussian.....	32
6a.	Plots of the Precipitating Electron Energy Flux and Characteristic Electron Energy.....	34
6b.	Plots of the Precipitating Electron Energy Flux for an Auroral Event on 29 December 1982.....	35
7a.	Same as Figure 5a but for a Quiet Aurora Late on 29 December 1982.....	36
7b.	Same as Figure 5b but for a Quiet Aurora Late on 29 December 1982.....	37
8.	Plot of Atmospheric Depth Versus Altitude (from Berger and Seltzer, 1972).....	46

FIGURES (Continued)

9a and b.	Plots of the Ratio of Bremsstrahlung Intensity at the Top of the Atmosphere To That at the Source Altitude as a Function of Zenith Angle for (a) 20 keV and (b) 6 keV.....	47
9c and d.	Plots of the Ratio of Bremsstrahlung Intensity at the Top of the Atmosphere To That at the Source Altitude as a Function of Zenith Angle for (c) 2 keV and (d) 1 keV.....	48

TABLES

1.	Energy Channels in keV.....	16
2.	X-ray Productivity for 0° Zenith Angle.....	17
3.	X-ray Productivity for 80° Zenith Angle.....	18

I. Introduction

To date, the energetic plasmas responsible for the terrestrial aurora have been probed directly with in situ spectral measurements of the precipitating electron flux, while the morphology and temporal behavior of the aurora have been monitored with ground-based and space-based imagery. Space-based X-ray imaging offers a means for combining spectral and spatial measurements of the aurora by detecting X-ray fluxes which arise from bremsstrahlung emission by the precipitating auroral electrons. Of course, the bremsstrahlung X-ray spectrum must be interpreted properly in order to infer the spectral parameters of the precipitating electrons. Quantitative interpretation of bremsstrahlung X-ray spectra is possible since the production and transport of > 1 keV bremsstrahlung X-rays in the atmosphere are reasonably well understood. Also, observations of bremsstrahlung X-rays have been accomplished (e.g., Mizera et al., 1978; Imhof et al., 1974, 1975a, b), and the most recent observations have provided two-dimensional images of the X-ray flux along with spectral measurements (e.g., Mizera et al., 1984; Imhof et al., 1982).

In practice, the use of bremsstrahlung spectral measurements to infer incident electron spectral parameters is hampered by instrumental limitations and low signal-to-noise ratio. Thus, a spectral deconvolution scheme which makes the most effective use of available data is required. The maximum entropy formalism (Jaynes, 1957) is a statistical technique which provides a statistically optimal estimator of a continuous quantity (in this case, the incident electron spectrum) when only a discrete set of integral functions of that quantity are known (namely, the observed X-ray spectrum). Maximum entropy analysis has been applied previously to image restoration problems (e.g., Andrews and Hunt, 1977; Gull and Daniell, 1978; Wilczek and Drapatz, 1985) where, for example, brightness images of astronomical objects appear noisy and

blurred due to inadequate detection equipment. The bremsstrahlung spectral deconvolution problem can be compared to noisy and blurred image restoration, since the electron-atmospheric interaction effectively causes "blurring" of the original electron spectral signature.

A numerical maximum-entropy deconvolution scheme has been developed which is specific to the bremsstrahlung problem. The technique includes a Chi-squared limitation on errors arising from statistical fluctuations in the X-ray flux measurements. The numerical technique has been applied to data acquired by the Aerospace X-ray spectrometer on the polar-orbiting DMSP-F6 spacecraft.

Section II of this report describes the formulation of the appropriate bremsstrahlung production function (i.e., the "blurring" or "response" function). Section III describes the maximum entropy constraints and derives a linear system of equations which comprise an interactive solution to the problem. Section IV applies the technique to some ideal and actual examples, and Section V summarizes the results.

II. Bremsstrahlung Production

It is necessary to determine an appropriate bremsstrahlung production function $\phi(X, T, \eta)$ which approximately satisfies the following expression for the observed X-ray spectrum:

$$f_x(X, \eta) = \int_x^{T_{MAX}} dT f_e(T) \cdot \phi(X, T, \eta) + e(X) \quad (1)$$

where the integral for the observed flux f_x as a function of X-ray energy X and aspect angle η (see Figure 1) must be carried to an incident electron energy T_{MAX} such that the contribution to observed X-ray flux from incident electron flux $f_{e0}(T_{MAX})$ is negligible. The factor $e(X)$ represents errors or variations which arise from processes not described by the production function ϕ . Later we assume that the errors $e(X)$ are not biased and represent, for example, fluctuations due to inadequate counting statistics. In practice the production integral (1) is replaced with a summation over energy levels T_i which are selected for evaluation. That is

$$f_{xk}(\eta) = \sum_{i=1}^n f_{ei} \cdot \phi_{i,k}(\eta) + e_k \quad (2)$$

The bremsstrahlung production kernel $\phi_{i,k}$ can be estimated based on analytical treatment of bremsstrahlung production and transport in the atmosphere (e.g., Luhmann, 1976; 1977) or from the results of Monte Carlo calculations (e.g., Seltzer and Berger, 1974). We review here an analytical technique for estimating observable X-ray flux at satellite altitudes in order to demonstrate some important physical considerations (limb brightening, for example). In any case, any appropriately derived bremsstrahlung production function $\phi_{i,k}$ can be substituted into the maximum entropy formulation described in Section III.

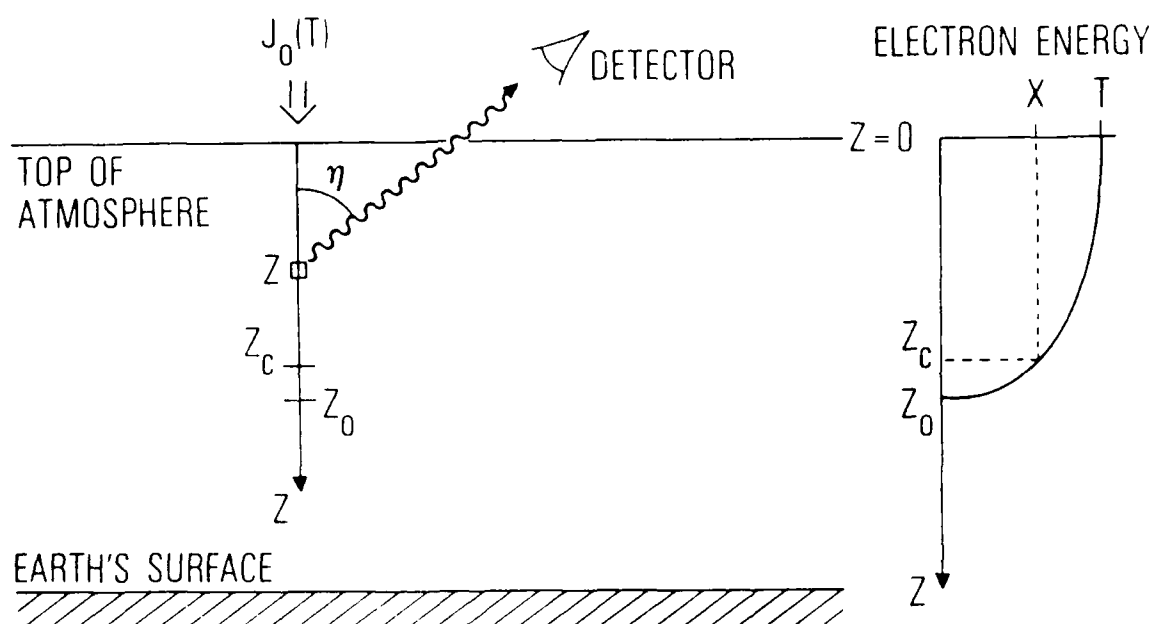


Figure 1. Plot Exhibiting the Plane-Parallel Geometry Used in All Computations in This Report. Atmospheric depth, z , increases downward, and z_c and z_0 indicate the emitting range and total range of an electron with initial energy T .

The bremsstrahlung production function $\phi_{i,k}$ represents the integrated X-ray productivity of an incident electron beam at energy T_i over an emission range $0 < z < z_c$ where z is the atmospheric depth (gm/cm^2). The form of $\phi_{i,k}$ must incorporate both electron energy degradation over the entire emission range and X-ray absorption over the escape path length $z \sec \eta$, where the angle η is the emission aspect angle with respect to the zenith. A plane parallel geometry can be assumed, as shown in Figure 1. Note that $f_e(T)$ must be assumed uniform over the "sensed" horizontal area.

Luhmann (1976) treated the spatial evolution of the energy spectrum of incident electrons on the atmosphere by showing that a solution to the Fokker-Planck equation for the electron distribution functions has the form

$$f_e(z, E) = \frac{2\pi}{v} \frac{dT/dS(T)}{dT/dS(E)} f_{eo}(T) \quad (3)$$

where

$$dT/dS(Y) = \frac{Y^{-3/4}}{7/4 B} \quad (4)$$

and

$$T = \left[\frac{1}{B} (z + BE^{7/4}) \right]^{4/7} \quad (5)$$

for a beam. Here Y is a dummy variable, E is the energy of the degraded beam and $B = 4.57 \times 10^{-6}$. The range of the beam is thus $z_0 = BT^{7/4}$, however it is more important to consider the emission range of the beam, beyond which an electron beam with initial energy T does not contribute to bremsstrahlung production at photon energy X . This range is such that $E = X$ in Eq. (5), or

$$z_c = B(T^{7/4} - X^{7/4}) \quad (6)$$

Similarly, one can determine the minimum incident electron energy which can contribute to bremsstrahlung emission at energy X for atmospheric depth z , which is

$$T_c = \left[\frac{1}{B} (z + BX^{7/4}) \right]^{4/7} \quad (7)$$

The flux spectrum of electrons at depth $0 < z < z_c$ is then just

$$f_e(z, E) = \left(\frac{E}{T} \right)^{3/4} f_{eo}(T) \Delta u \quad (8)$$

where Δu is the cosine of the beam width in pitch angle.

The bremsstrahlung production rate due to an electron of energy E is determined by the Bethe-Heitler differential cross section (Heitler, 1954), which for an air target of mean atomic weight M takes the form

$$\frac{1}{M} \frac{d\sigma_B}{dX}(X, E) = \frac{1.75}{XE} \ln \left[\frac{(\sqrt{E} + \sqrt{E-X})^2}{X} \right] \quad (9)$$

with units $\text{cm}^2/\text{g keV}$. This cross section is plotted in Figure 2 for selected electron energies. Note that high energy electrons contribute significantly to X-ray production at much lower energies.

The bremsstrahlung production rate at atmospheric depth z is thus

$$P_B(z, X) = \frac{\Omega \Delta u}{M} \int_{T_c}^{\infty} dT \frac{d\sigma_B}{dX}(X, E) \left(\frac{E}{T} \right)^{3/4} f_{eo}(T) \quad (10)$$

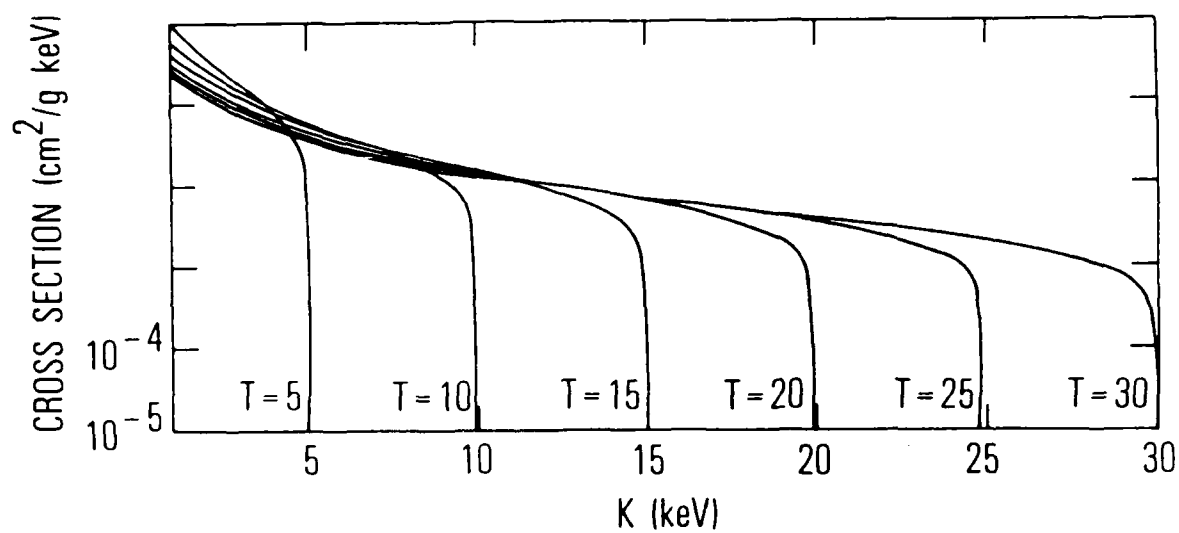


Figure 2. Plot of the Bethe-Heitler Cross Section for an Air Target.
Curves are drawn for a number of electron energies T.

where the factor of Ω arises from an integration over the angular distribution of bremsstrahlung emission with respect to the direction of the electron beam. Since we are concerned with auroral energies only, the slight energy dependence in the emission angular distribution (Rees, 1964) has been ignored here, and for an electron beam we use $\Omega = 2/\pi^2$. Equation 10 is written intentionally as an integral over incident energy T rather than local degraded energy E in order to facilitate later numerical evaluation of $J_{e0}(T)$.

The bremsstrahlung intensity viewed from the top of the atmosphere is the productivity function given in Eq. (10) multiplied by an exponential attenuation factor and integrated along the appropriate propagation path from the maximum source depth z_c to the top of the atmosphere (see also Luhmann, 1977):

$$f_X(X, \eta) = \int_0^{z_c \sec \eta} dz \sec \eta P_B(z, X) \exp(-\mu_a z \sec \eta) \quad (11)$$

where $\mu_a = \mu_a(X)$ is the mass absorption coefficient which for $1 \text{ keV} < X < 30 \text{ keV}$ can be approximated

$$\mu_a(X) = 4.28 \times 10^3 X^{-3.0} \text{ cm}^2/\text{g} \quad (12)$$

for a nitrogen/oxygen atmosphere [from the data of Hubbell (1971)].

It is convenient, for our purposes, to evaluate equations (10) and (11) for discrete energy levels $X = K_i$; $i = 1, m$. Also, we choose to evaluate $f_e(T)$ at these same energy levels $T = K_i$; $i = 1, m$. It is necessary at this point to specify the relationship between energy levels K_i and differential energy intervals ΔK_i in order to evaluate equation (10) numerically. Here we apply a geometric progression of energy levels which is characteristic of current instrumentation. Namely,

$$K_{i+1}/K_i = 1 + \Delta \quad (13a)$$

$$\Delta K_i = \Delta \cdot K_i \quad (13b)$$

where Δ is typically between 0.15 and 0.20. In doing this, tabular values of $\phi_{i,j}$, computed for a range of zenith angles, are specific to the energy increments K_j but are otherwise universal. Examples of $\phi_{i,j}$ values computed for $\eta = 0^\circ$ and $\eta = 80^\circ$ are shown in Tables 2 and 3 for values of K_j listed in Table 1. These values are also displayed in graphic form in Figure 3. The plot depicts the contribution of unit incident flux of electrons at energy T to observable X-ray flux at energy K . Note, for example, the characteristic turnover of the production function at low X-ray energies for high incident electron energy. This is due to re-absorption of low energy X-rays which are emitted from deep within the atmosphere by deeply penetrating high energy electrons. It is useful to note that a reasonable approximation to the production function, neglecting soft X-ray reabsorption, is

$$\phi_{i,j} = 4.86 \times 10^{-6} \frac{(T_i - K_j) T_i}{K_j^{1.5}} \quad (14)$$

Of course, this approximate form applies equally well to energy levels other than those specified in equation (13). A discussion of aspect-angle effects such as limb-brightening or darkening appears in an Appendix.

Table 1. Energy Channels in keV

Channel Number	Energy (keV)	Channel Number	Energy (keV)
1	2.00	9	7.36
2	2.35	10	8.86
3	2.77	11	10.2
4	3.26	12	12.0
5	3.84	13	14.1
6	4.51	14	16.6
7	5.36	15	19.6
8	6.25	16	23.0

Table 2. X-ray Productivity for 0° Zenith Angle

	1	2	3	4	5	6	7	8	9	10	11	12	13	14	15	16
1	0	.31200(-3)	.17600(-3)	.39000(-3)	.76000(-3)	.12000(-3)	.20150(-3)	.30301(-3)	.42201(-3)	.53007(-3)	.64131(-3)	.76060(-3)	.87451(-3)	.10001(-3)	.10001(-3)	.31127(-3)
2	0	0	.39721(-3)	.20411(-3)	.63711(-3)	.00900(-3)	.16501(-3)	.23120(-3)	.30200(-3)	.37397(-3)	.43301(-3)	.50001(-3)	.57101(-3)	.63131(-3)	.68991(-3)	.30934(-3)
3	0	0	0	.66220(-3)	.21051(-3)	.51110(-3)	.97011(-3)	.16627(-3)	.26462(-3)	.40523(-3)	.60001(-3)	.81000(-3)	.11000(-3)	.16117(-3)	.21010(-3)	.20111(-3)
4	0	0	0	0	.76021(-3)	.23700(-3)	.30500(-3)	.10931(-3)	.10700(-3)	.30220(-3)	.60001(-3)	.69710(-3)	.10000(-3)	.10001(-3)	.10121(-3)	.39510(-3)
5	0	0	0	0	0	.01201(-3)	.26401(-3)	.65220(-3)	.12431(-3)	.21101(-3)	.36001(-3)	.51370(-3)	.70001(-3)	.11501(-3)	.10410(-3)	.22711(-3)
6	0	0	0	0	0	0	.00331(-3)	.33101(-3)	.35000(-3)	.14100(-3)	.24301(-3)	.39301(-3)	.61001(-3)	.91051(-3)	.13300(-3)	.10130(-3)
7	0	0	0	0	0	0	0	.10091(-3)	.37370(-3)	.64100(-3)	.15007(-3)	.37000(-3)	.60551(-3)	.90371(-3)	.10400(-3)	.13301(-3)
8	0	0	0	0	0	0	0	.12370(-3)	.43921(-3)	.90201(-3)	.90201(-3)	.10170(-3)	.31201(-3)	.50001(-3)	.70100(-3)	.11971(-3)
9	0	0	0	0	0	0	0	.13070(-3)	.60231(-3)	.60231(-3)	.10001(-3)	.10001(-3)	.20531(-3)	.35010(-3)	.57370(-3)	.00971(-3)
10	0	0	0	0	0	0	0	0	0	.15000(-3)	.15000(-3)	.30000(-3)	.13201(-3)	.23351(-3)	.60111(-3)	.03100(-3)
11	0	0	0	0	0	0	0	0	0	0	0	.17700(-3)	.61200(-3)	.13050(-3)	.20331(-3)	.05000(-3)
12	0	0	0	0	0	0	0	0	0	0	0	0	.20037(-3)	.00000(-3)	.15001(-3)	.20700(-3)
13	0	0	0	0	0	0	0	0	0	0	0	0	0	.22710(-3)	.70500(-3)	.17731(-3)
14	0	0	0	0	0	0	0	0	0	0	0	0	0	0	.20030(-3)	.00971(-3)
15	0	0	0	0	0	0	0	0	0	0	0	0	0	0	0	.20100(-3)
16	0	0	0	0	0	0	0	0	0	0	0	0	0	0	0	0

Table 3. X-ray Productivity for 80° Zenith Angle

λ	1	2	3	4	5	6	7	8	9	10	11	12	13	14	15	16
1	0	.00306(-3)	.31010(-1)	.70027(-4)	.13066(-3)	.33071(-3)	.37064(-3)	.30700(-3)	.00271(-3)	.13316(-1)	.10230(-1)	.37051(-1)	.10633(-1)	.32076(-1)	.71059(-1)	.00097(-1)
2	0	0	.10420(-1)	.37012(-4)	.00061(-1)	.13194(-3)	.20421(-3)	.07751(-3)	.07010(-3)	.10370(-1)	.33123(-1)	.23003(-1)	.31493(-1)	.60101(-1)	.61021(-1)	.00121(-1)
3	0	0	0	.11610(-1)	.00166(-1)	.00121(-1)	.17256(-3)	.20420(-3)	.00370(-3)	.70117(-1)	.11540(-1)	.17107(-1)	.35021(-1)	.33076(-1)	.00931(-1)	.71155(-1)
4	0	0	0	0	.11230(-1)	.03001(-1)	.10701(-3)	.13300(-3)	.33000(-3)	.00701(-1)	.00061(-1)	.13000(-1)	.10471(-1)	.20401(-1)	.01061(-1)	.00001(-1)
5	0	0	0	0	0	.10320(-1)	.31516(-1)	.11300(-3)	.21010(-3)	.37009(-1)	.01901(-1)	.07126(-1)	.14700(-1)	.32076(-1)	.32331(-1)	.00773(-1)
6	0	0	0	0	0	0	.17101(-1)	.30113(-1)	.13130(-3)	.30007(-1)	.01771(-1)	.70361(-1)	.11031(-1)	.10031(-1)	.20121(-1)	.34000(-1)
7	0	0	0	0	0	0	0	.10400(-1)	.03130(-1)	.14713(-1)	.20054(-1)	.00401(-1)	.70100(-1)	.12633(-1)	.00061(-1)	.20101(-1)
8	0	0	0	0	0	0	0	0	.21010(-1)	.70100(-1)	.30709(-1)	.31031(-1)	.35020(-1)	.00000(-1)	.10111(-1)	.31070(-1)
9	0	0	0	0	0	0	0	0	.20110(-1)	.03130(-1)	.03066(-1)	.10011(-1)	.15003(-1)	.02102(-1)	.10131(-1)	.13040(-1)
10	0	0	0	0	0	0	0	0	0	0	.07510(-1)	.00703(-1)	.31371(-1)	.00101(-1)	.70100(-1)	.11000(-1)
11	0	0	0	0	0	0	0	0	0	0	0	.30764(-1)	.10456(-1)	.20097(-1)	.03707(-1)	.37007(-1)
12	0	0	0	0	0	0	0	0	0	0	0	0	.30021(-1)	.12073(-1)	.07060(-1)	.01001(-1)
13	0	0	0	0	0	0	0	0	0	0	0	0	0	.10462(-1)	.13054(-1)	.30091(-1)
14	0	0	0	0	0	0	0	0	0	0	0	0	0	0	.00330(-1)	.13040(-1)
15	0	0	0	0	0	0	0	0	0	0	0	0	0	0	0	.00356(-1)
16	0	0	0	0	0	0	0	0	0	0	0	0	0	0	0	0

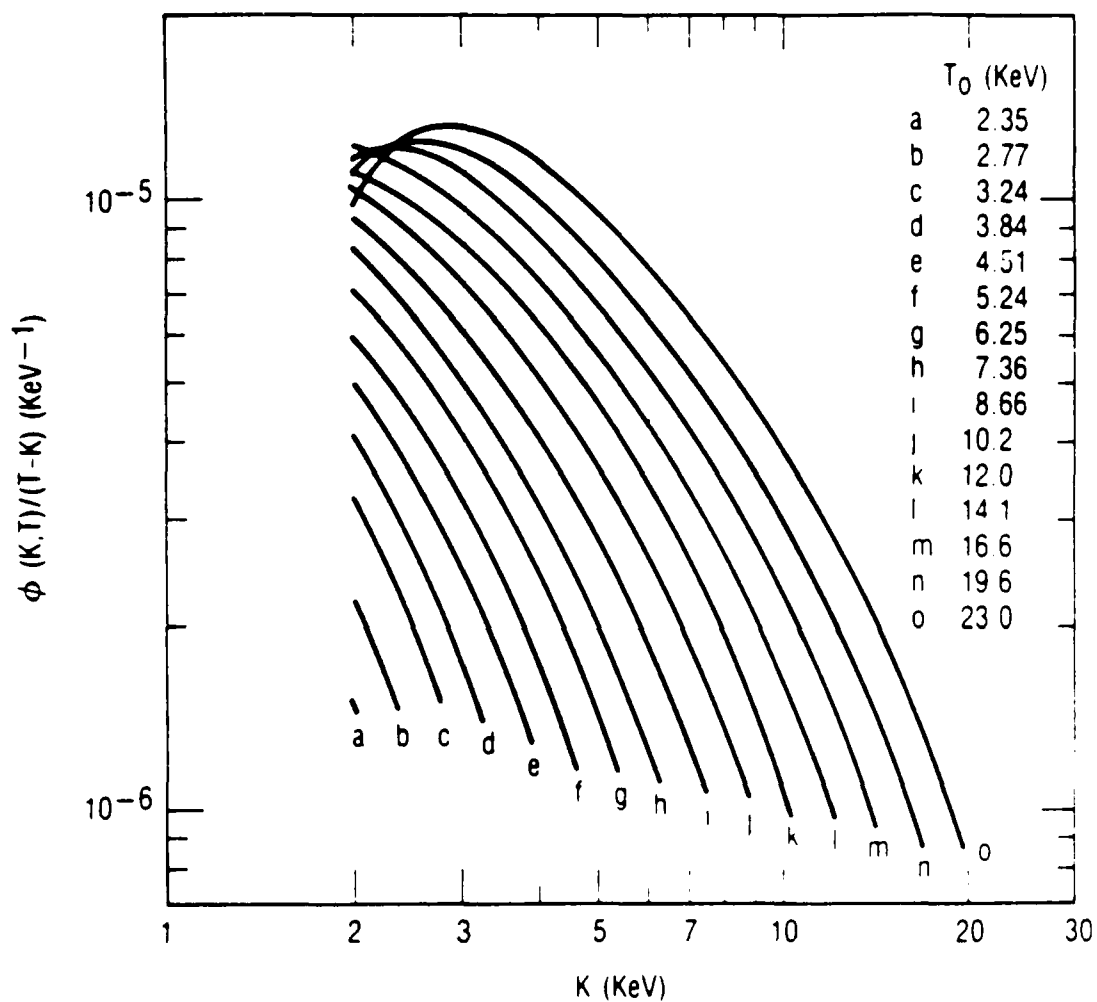


Figure 3. Plot of the Bremsstrahlung Production at Energy K of Unit Incident Electron Flux at Energy T for a Geometric Progression of Energy Channels

III. Maximum Entropy Deconvolution

The bremsstrahlung production function computed in the previous section (or any other appropriate kernel $\phi_{i,j}$) can be used to compute the observable X-ray flux at satellite altitudes caused by incident electron flux with spectrum $f_e(T)$. In this section a deconvolution scheme is presented which enables the computation of the incident electron spectrum based on discrete observations of the bremsstrahlung flux. The technique presented here resembles similar maximum-entropy schemes which have been developed for image restoration (see, for example, Gull and Daniell, 1978; Wilczek and Drapatz, 1985). The similarity in these data analysis techniques is to be expected, since entropy maximization generally provides the smoothest (i.e., most cautious) estimate of a distribution among a set of distributions which are allowed under constraints imposed by observations. Below we describe the constraint equations appropriate to the bremsstrahlung problem and develop a maximum entropy deconvolution scheme for the incident electron flux spectrum.

As in Section II, we assume that discrete observations of the bremsstrahlung X-ray flux $f_x(X_k)$ are available, and that these measurements are related to the incident electron flux through the following convolution function:

$$f_{xk} = \sum_{i=1}^n \phi_{i,k} \cdot f_{ei} + e_k \quad (15)$$

Here the e_k terms represent errors, which we will assume to arise from statistical counting deviations. This assumption requires an estimate of the standard deviations of e_k , which we call σ_k . Gull and Daniell (1978) suggest the application of a χ^2 constraint to the errors e_k when their variances σ_k^2 are known. That is

$$\sum_{k=1}^m \frac{e_k^2}{\sigma_k^2} = \Delta^2 \quad (16)$$

The constraint Δ^2 can be chosen to reflect a confidence level p by setting Δ^2 to the value of the inverse χ^2 distribution function with m degrees of freedom.

Finally, the entropy of the incident electron distribution is defined by the Shannon form.

$$S = - \sum_{i=1}^m f_{ei} \ln f_{ei} \quad (17)$$

We wish to find the distribution f_{ei} which maximizes equation (17) under the constraints of equations (15) and (16). The Lagrangian of this system has the form

$$\begin{aligned} L(f_{e1} \dots f_{en}, e_1 \dots e_m, \beta_0 \dots \beta_{m+1}) = \\ = - \sum_{i=1}^m f_{ei} \ln f_{ei} - \beta_0 \left[\sum_{i=1}^n f_{ei} - n f_{e0} \right] - \\ - \sum_{k=1}^m \beta_k \left[\sum_{i=1}^n \phi_{i,k} f_{ei} - f_{xk} - e_k \right] - \beta_{m+1} \left[\sum_{k=1}^m \frac{e_k^2}{\sigma_k^2} - \Delta^2 \right] \end{aligned} \quad (18)$$

where f_{e0} represents an "average" flux which can be estimated from the integrated X-ray flux, then adjusted in later iterations using a continuation technique. Differentiating the Lagrangian with respect to f_{ei} and e_k , and setting the partial derivatives equal to zero, we get the following set of $n + m$ equations

$$\ln f_{ei} = -1 - \beta_0 - \sum_{k=1}^m \beta_k \phi_{i,k}, \quad i = 1, \dots, n \quad (19)$$

$$e_k = \beta_k \frac{\alpha_k^2}{2\beta_{k+1}} \quad (20)$$

Solving for f_{ei} ,

$$f_{ei}(\beta_1 \dots \beta_m) = n f_{e0} \frac{\exp\left[-\sum_{k=1}^m \beta_k \phi_{i,k}\right]}{\sum_{\ell=1}^n \exp\left[-\sum_{k=1}^m \beta_k \phi_{\ell,k}\right]} \quad (21)$$

and substituting f_{ei} and e_k into equations (15) and (16) we get the set of $m + 1$ nonlinear equations for the Lagrangian coefficients β_k

$$F_k = \sum_{i=1}^n \phi_{i,k} f_{ei}(\beta_1 \dots \beta_m) - \beta_k \frac{\alpha_k^2}{2\beta_{k+1}} - f_{xk} = 0 \quad k = 1, \dots, m \quad (22)$$

$$F_{m+1} = \frac{1}{4\beta_{m+1}^2} \sum_{k=1}^m \alpha_k^2 \beta_k^2 - \Delta^2 = 0 \quad (23)$$

The system of equations (22) and (23) can be solved iteratively using a nonlinear Newton's method. The Jacobian of the system is given by $J_{kj} = \partial F_k / \partial \beta_j$, where

$$J_{kj} = \sum_{i=1}^n \phi_{i,k} \frac{\partial f_{ei}}{\partial \beta_j} - \delta_{kj} \frac{\alpha_k^2}{2\beta_{m+1}^2} \quad \begin{cases} k = 1, \dots, m \\ j = 1, \dots, m \end{cases}$$

$$J_{kj} = \beta_k \frac{\alpha_k^2}{2\beta_{m+1}^2} \quad \begin{cases} k = m+1 \\ j = 1, \dots, m \end{cases}$$

$$\begin{aligned}
J_{kj} &= \beta_j \frac{\sigma_1^2}{2\beta_{m+1}^2} \\
J_{kj} &= \frac{1}{2\beta_{m+1}^3} \sum_{l=1}^m \sigma_l^2 \beta_l^2
\end{aligned}
\quad \left\{ \begin{array}{l} k = m+1 \\ j = 1, \dots, m \end{array} \right. \quad (24)$$

The iteration equation is then

$$\vec{J}(\vec{\beta}^{(1)} - \vec{\beta}^{(0)}) - \vec{F} = 0 \quad (25)$$

which represents a linear system in $\beta_k^{(1)}$. Following Wilczek and Drapatz (1985), the starting points are calculated from the initialization equations:

$$f_{e0} \sum_{i=1}^m \phi_{i,k} - \beta_k^{(0)} \frac{\sigma_k^2}{2\beta_{m+1}^{(0)}} - f_{xk} = 0 \quad k = 1, \dots, m \quad (26)$$

$$f_{ei}(\beta_1^{(0)} \dots \beta_m^{(0)}) = f_{ei}(0 \dots 0) = f_{e0} \quad (27)$$

In test cases with 16 discrete measurement channels and $f_{xk}/\sigma_k = 10$ with a confidence level of 0.9, this scheme has been found to converge in approximately ten iterations. Some examples are discussed in the following section. It should be noted that the solution set of equation (25) allows an easy "plug-in" of different forms for the bremsstrahlung production function ϕ . Thus, the deconvolution scheme can be modified easily if new or better forms for the production function become available.

IV. Examples

In this section, the deconvolution scheme described earlier is applied to bremsstrahlung X-ray spectra which are characteristic of the earth's aurora. The first examples are "ideal" in that they depict the ability of the deconvolution technique to reproduce the shape of Maxwellian and Gaussian electron spectra. These examples do not include instrumental effects, although random noise is applied to the "ideal" signal in order to demonstrate the effects of noise on the numerical technique. These first examples are meant to give the reader a "feel" for the actual performance characteristics of the numerical scheme. The second set of examples simulates the response of an actual instrument (The Aerospace scanning X-ray spectrometer SSB/A on DMSP-F6) to ideal spectra. The "noise" added in these cases is characteristic of counting statistics variations, and consequently is energy dependent. The final examples compare spectral parameters inferred from actual bremsstrahlung measurements in the aurora with parameters observed directly by a particle detector. These final examples show the performance of the deconvolution scheme in the "real world."

Figures 4a-c show examples of the ability of the numerical scheme described in Section III to reproduce ideal spectral shapes. Three examples are shown: a 1 keV Maxwellian, a 10 keV Maxwellian, and a 5 keV Maxwellian with an added 2σ 10 keV Gaussian peak. In these examples, the observable X-ray flux from each input spectrum is calculated using equation (2) and the bremsstrahlung production function derived in Section II. A simple geometric progression of 16 energy channels between 1 and 30 keV is assumed. Random noise is added to this ideal signal at the 3, 10 and 30% level. The noisy X-ray spectrum is then deconvoluted by the method described in Section III. A

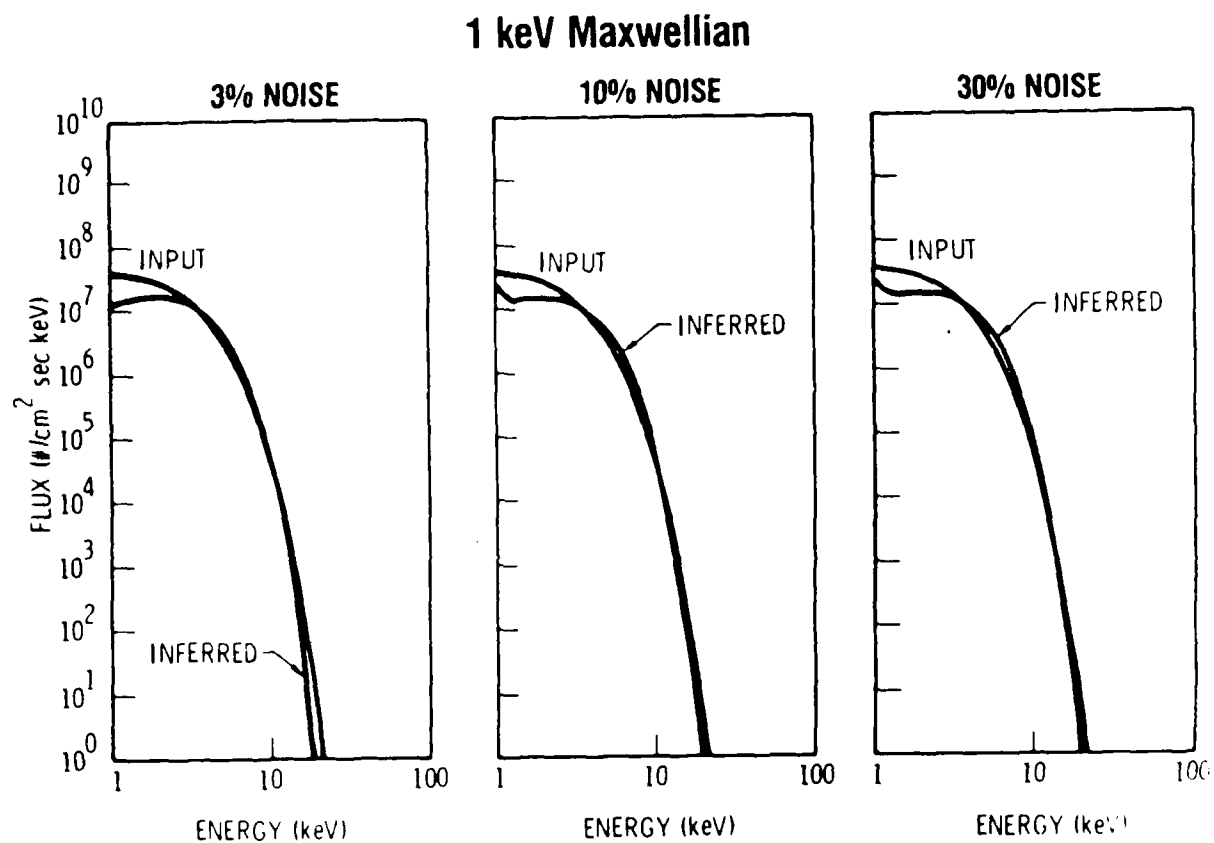


Figure 4a. Plots of Input and Inferred Electron Spectra for 1 keV Maxwellian

10 keV Maxwellian

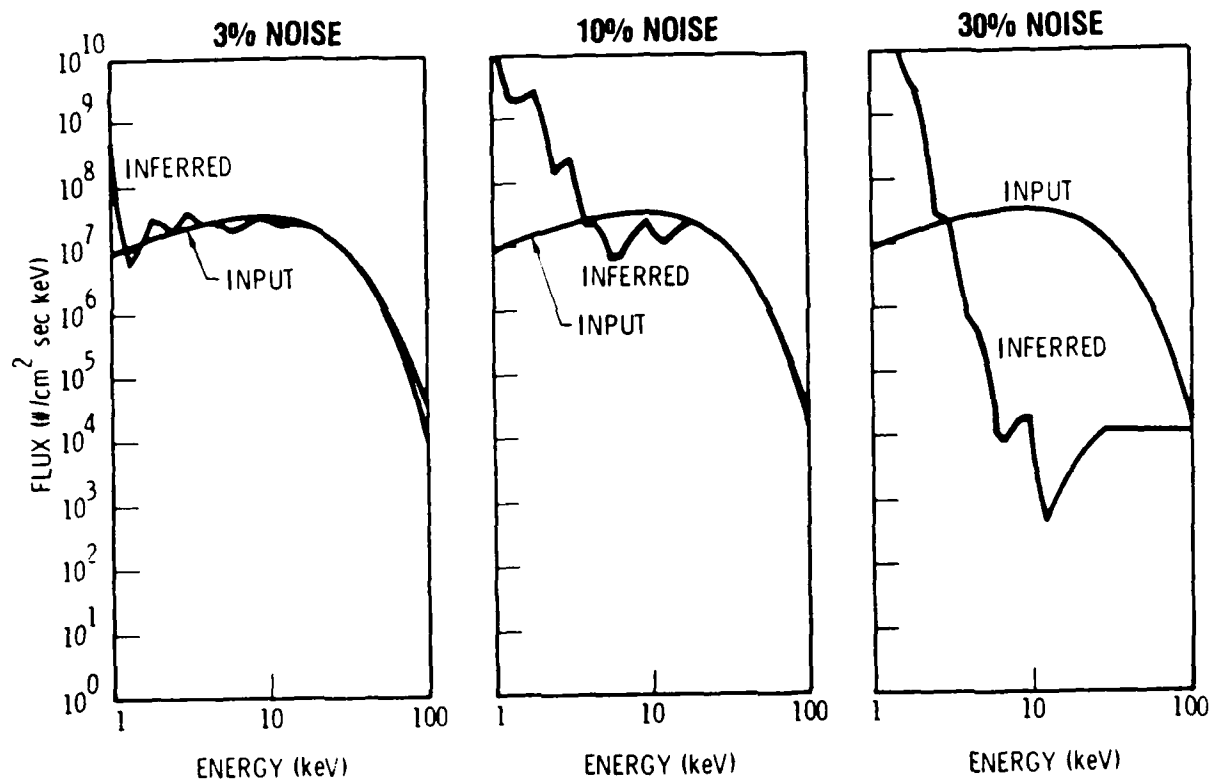


Figure 4b. Plots of Input and Inferred Electron Spectra for 10 keV Maxwellian.

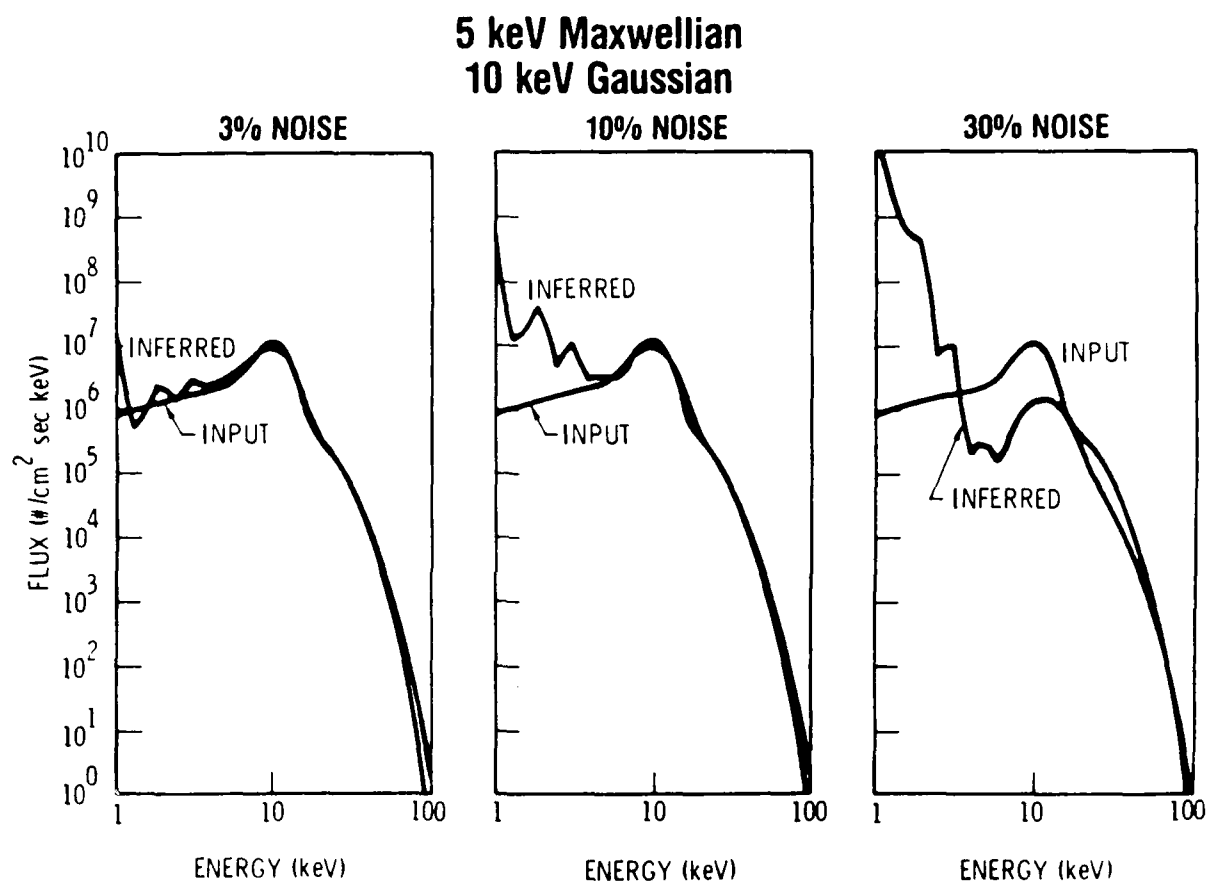


Figure 4c. Plots of Input and Inferred Electron Spectra for 5 keV Maxwellian with a 10 keV $\sigma = 2$ Gaussian Peak

continuous inferred electron spectrum is computed for energies between 1 and 100 keV. The results shown in Figures 4a-c are for ten iterations - no substantial improvement was found at higher iterations.

It is obvious at a glance that the deconvolution works particularly well for the steep 1 keV spectrum, even at high noise level. This characteristic is easy to understand if one thinks of the input spectrum as a simple signal distribution - the 1 keV spectrum represents a sharper signal than the smoother, harder spectra. A second obvious characteristic of the deconvolution is its difficulty in reproducing the low-energy portion of very hard (e.g., 10 keV) spectra under even modest noise conditions. This problem is due primarily to the shape of the bremsstrahlung production function itself. It is a characteristic of the bremsstrahlung process that energetic electrons produce much higher fluxes of low energy X-rays than do low energy electrons. The low energy X-ray signal is partially masked by X-rays resulting from the high energy portion of the incident electron spectrum, and information is lost due to decreased signal-to-noise ratio at low energies. This effect is also apparent in Figure 4c, where the deconvolution technique has difficulty reproducing the electron spectral shape below the Gaussian peak energy. All in all, the deconvolution scheme produces good results for noise levels below about 10%.

Figures 5a-c show the results obtained for the same input spectra as in Figures 4a-c, but for a response which simulates that of an actual proportional counter. (The Aerospace Corporation scanning X-ray spectrometer carries a proportional counter with geometric factor of $.03 \text{ cm}^2 \text{ ster}$ and energy channels as listed in Table 1. Measurements of auroral X-ray spectra are obtained once per second at an altitude of 830 km.) Naturally, for these spectra the statistical "noise" is energy-channel dependent, with larger

Simulated DMSP-F6 SSB/A Response **1 keV MAXWELLIAN**

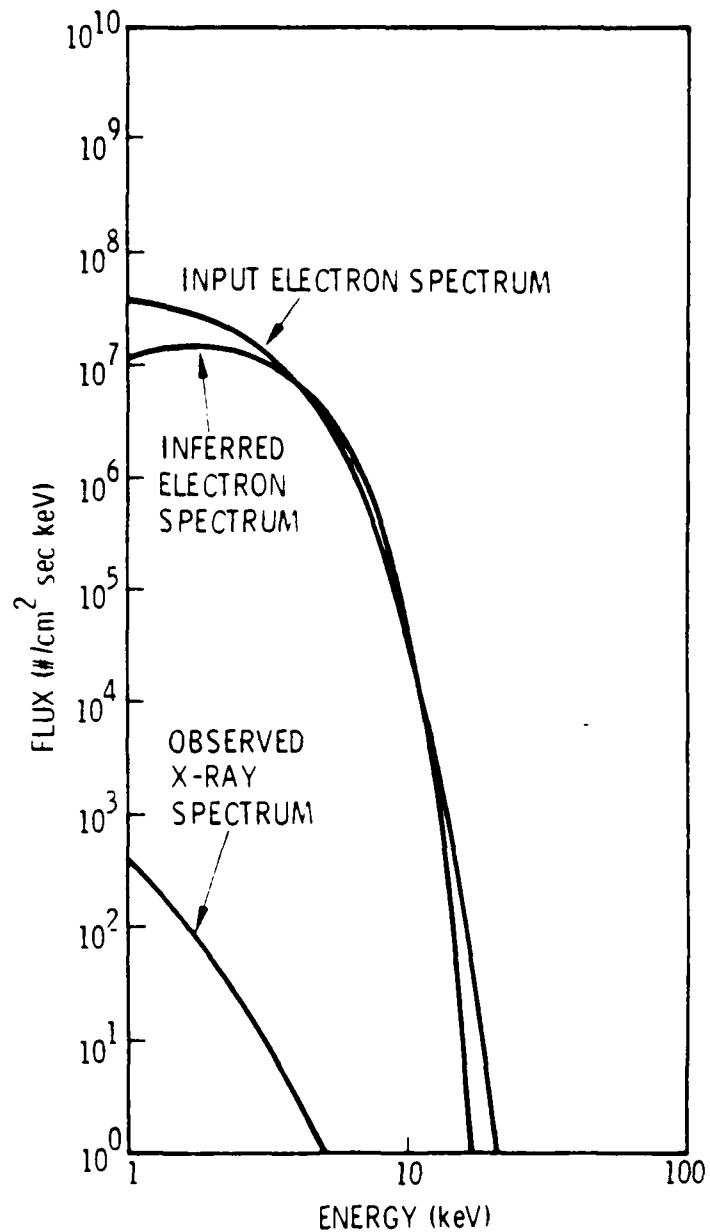


Figure 5a. Plots of Input and Inferred Electron Spectra Incorporating a Simulated Instrumented Response to the Observed X-Ray Spectra for 1 keV Maxwellian

Simulated DMSP-F6 SSB/A Response **10 keV MAXWELLIAN**

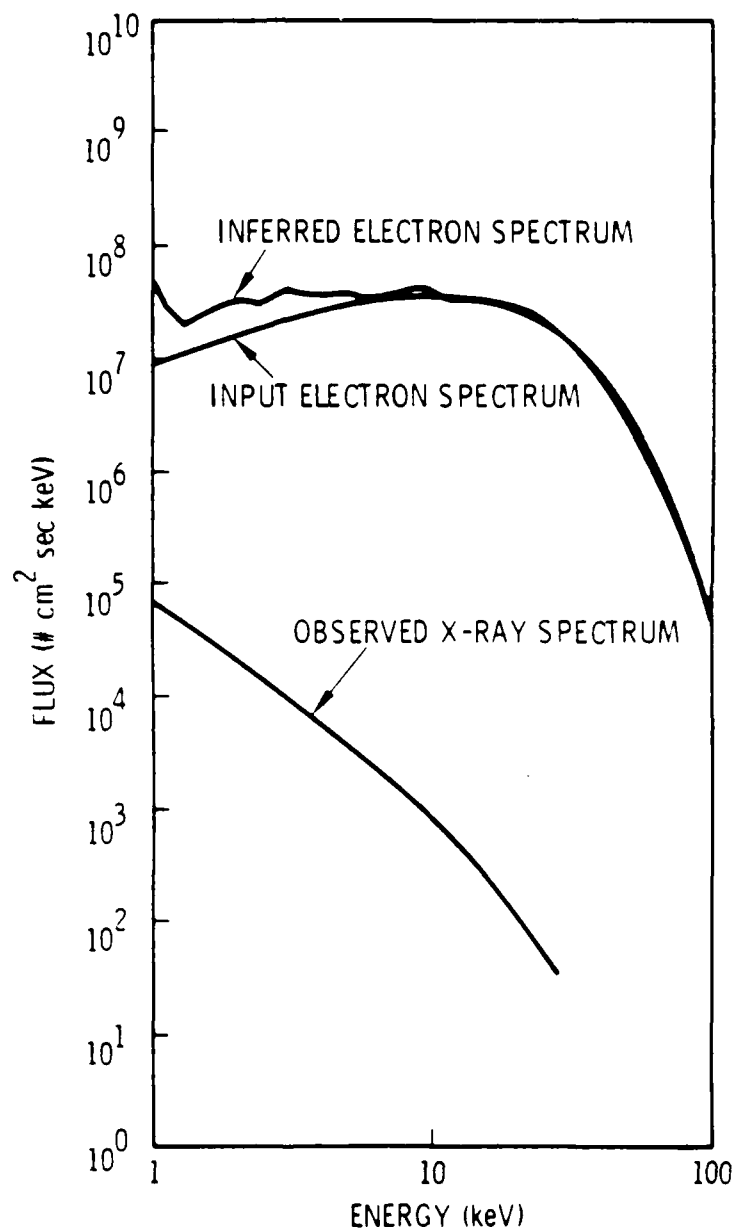


Figure 5b. Plots of Input and Inferred Electron Spectra Incorporating a Simulated Instrument Response to the Observed X-Ray Spectra for 10 keV Maxwellian

Simulated DMSP-F6 SSB/A Response

5 keV MAXWELLIAN

10 keV GAUSSIAN

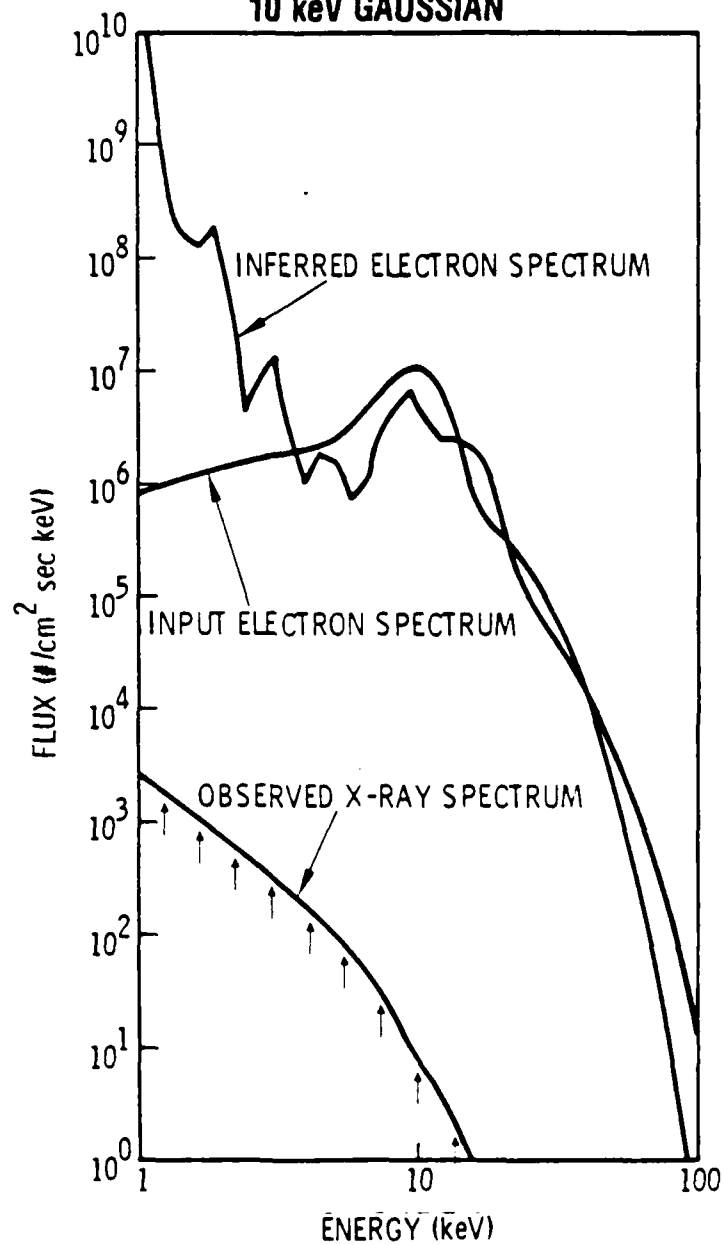


Figure 5c. Plots of Input and Inferred Electron Spectra Incorporating a Simulated Instrument Response to the Observed X-Ray Spectra for 5 keV Maxwellian with a 10 keV $\sigma = 2$ Gaussian

relative errors occurring in the higher energy channels. However, because of the skewed form of the bremsstrahlung production function these errors manifest themselves primarily in the low-energy portion of the inferred electron spectrum. Again, soft spectra are better represented than hard spectra or spectra with peaks, although reasonable results were obtained for all of the examples shown here. Of course, better results would be obtained with instruments having larger geometric factors, with which statistical errors could be decreased.

Figures 6a, b and 7a, b show results obtained using actual auroral X-ray data acquired by the Aerospace scanning X-ray spectrometer. Fortunately the DMSP-F6 satellite, launched in December 1982 into a polar, circular orbit at 840 km altitude, carried both the Aerospace scanning auroral X-ray spectrometer and a precipitating auroral electron detector. This instrumentation allows a good test of the computational procedure described in the previous section. While the Aerospace X-ray spectrometer is a raster scanning instrument, the data used in this discussion is taken from periods when the instrument was in a static nadir-pointing mode. This permits a more detailed comparison with the precipitating electron data. The electron data is from the J-package instrument provided by the Air Force Geophysics Laboratory, which provides a precipitating electron spectrum once per second over the energy range $30 \text{ eV} < T < 30 \text{ keV}$. Only the data from $T \geq 2 \text{ keV}$ will be used here.

In order to compare the observed and inferred electron spectra we have chosen to deal with the fundamental spectral parameters; integral energy flux (ETOT), integral number flux (JTOT) and characteristic energy (EO), defined below:

$$ETOT = \alpha \int_{2 \text{ keV}}^{30 \text{ keV}} dT J_o(T) T \quad \text{erg/cm}^2 \text{ sec}$$

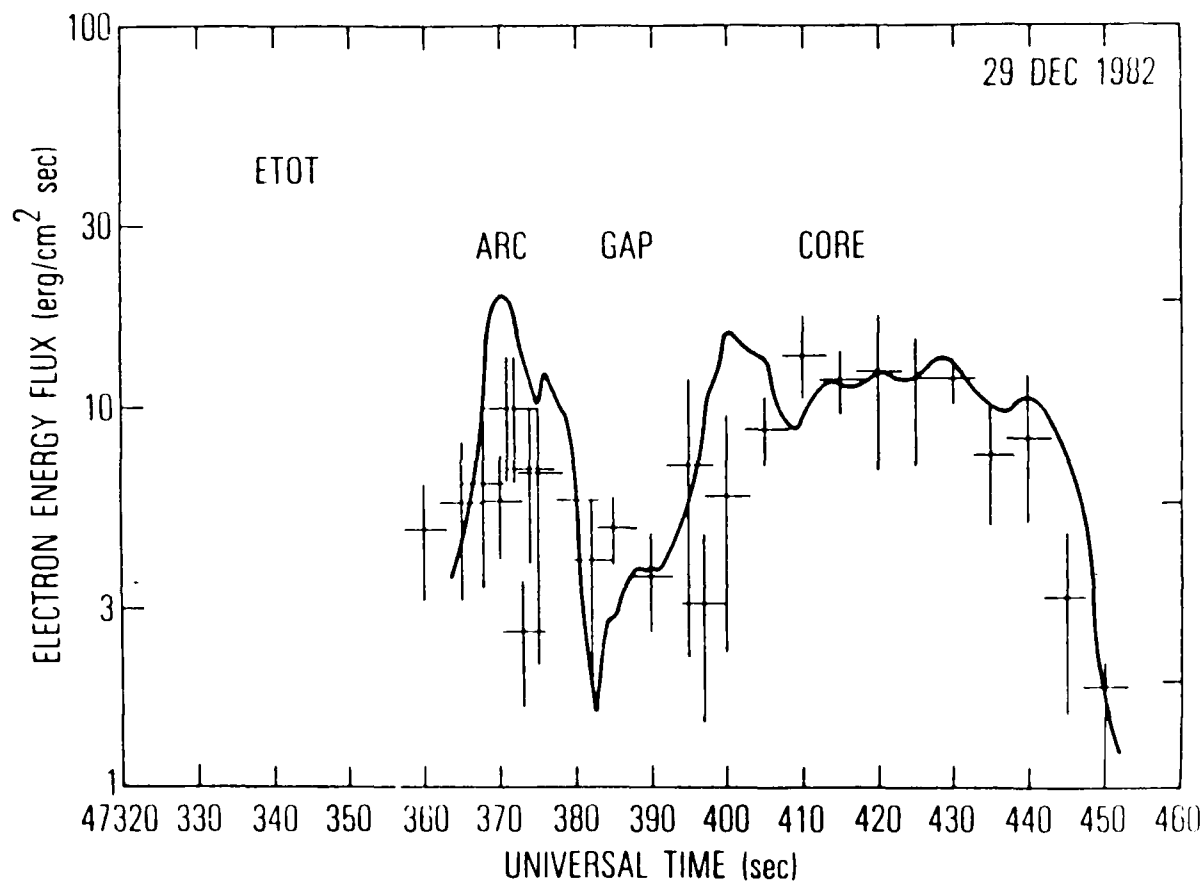


Figure 6a. Plots of the Precipitating Electron Energy Flux and Characteristic Electron Energy. The solid line reveals spectral parameters computed from direct observations of the precipitating electrons that cross indicate quantities inferred from bremsstrahlung X-ray observations.

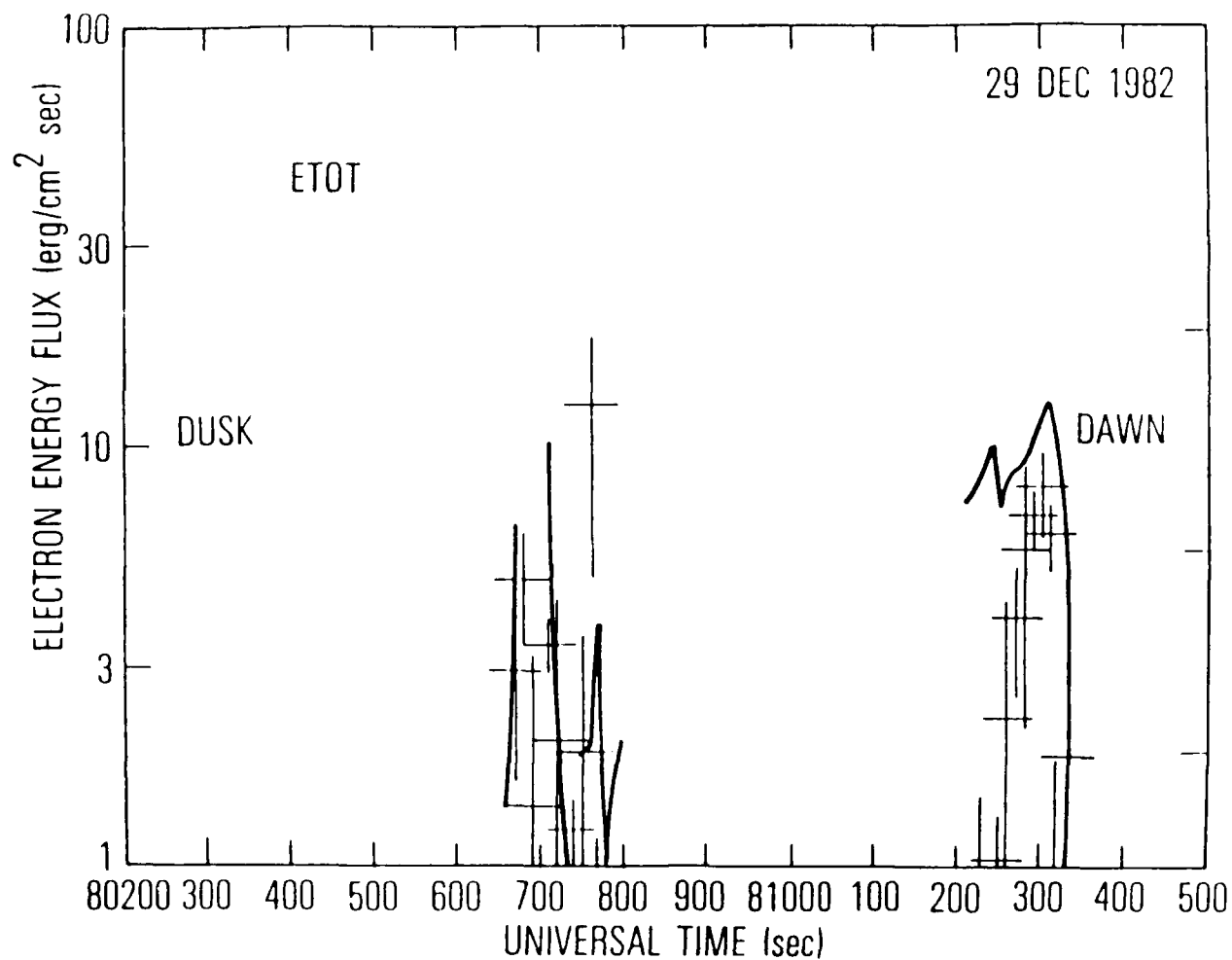


Figure 7a. Same as Figure 5a but for a Quiet Aurora Late on 29 December 1982. Note that this example includes both dawn and dusk aurora.

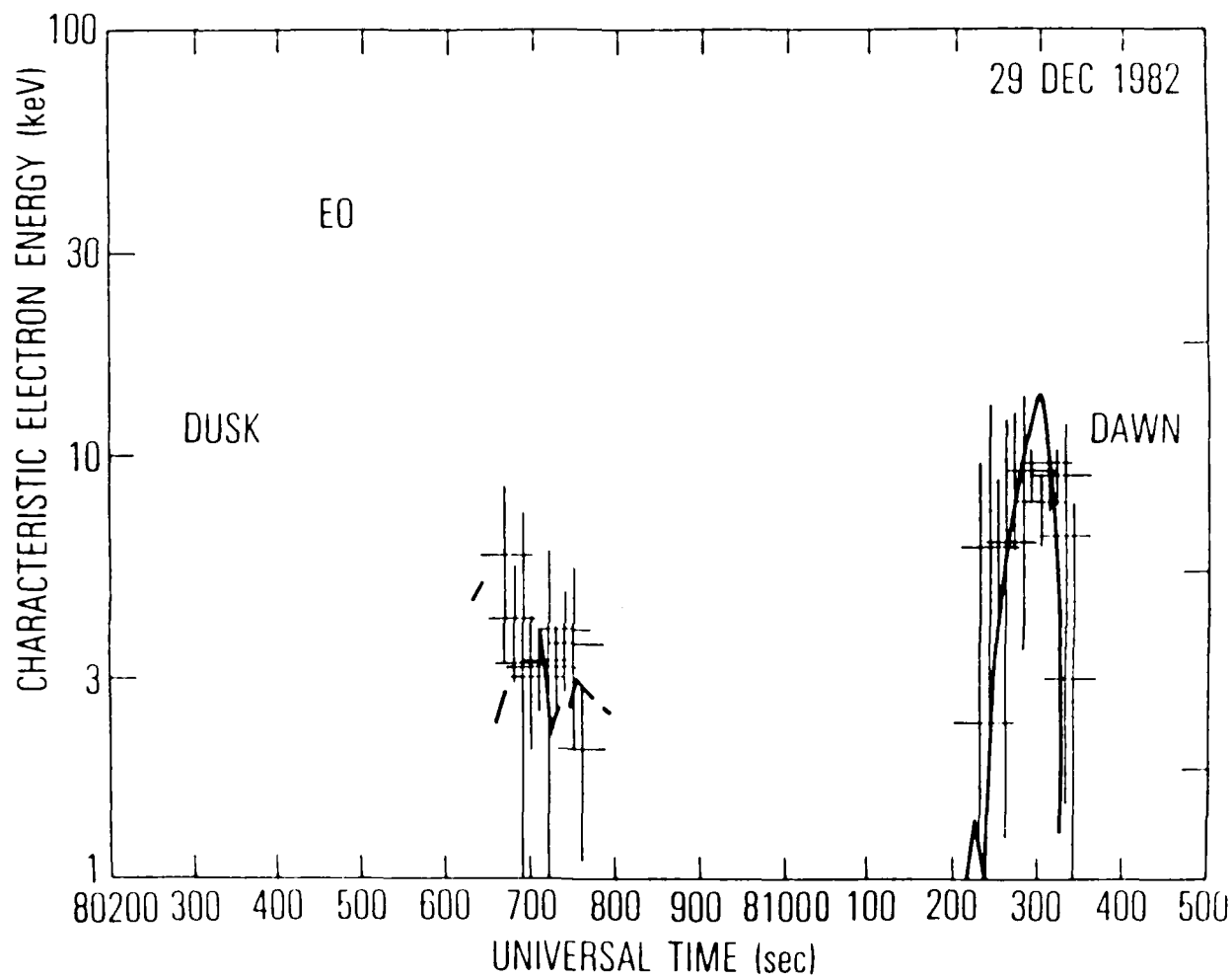


Figure 7b. Same as Figure 5b but for a Quiet Aurora Late on 29 December 1982. Note that this example includes both dawn and dusk aurora.

$$J_{TOT} = \int_{2 \text{ keV}}^{30 \text{ keV}} dT J_o(T) \quad \#/\text{cm}^2 \text{ sec} \quad (28)$$

$$E_0 = \frac{1}{\alpha} \frac{E_{TOT}}{J_{TOT}} \quad \text{keV}$$

where $\alpha = 1.602 \times 10^{-9}$. These spectral parameters are also important in that they are used often as the basis of other empirically derived relations, such as ionospheric conductance.

Two samples of data were chosen for study. The first, acquired on 29 December 1982 between 47320-47460 seconds UT in the dusk sector, is characteristic of an auroral surge. The second, acquired on 29 December 1982 between 80200 - 81500 seconds UT is more characteristic of a quiet aurora, and includes auroral data from both the dusk and dawn sectors. The first event occurred in darkness, while the second was in full sunlight.

Figures 6a, b show the observed and inferred electron spectral parameters from the active auroral surge event. The satellite proceeded from high toward low latitude during this event. The DMSP optical imagery revealed that the satellite passed over a bright, narrow arc at high latitudes before encountering a broad core of a westward-travelling surge between 47400-47450 UT. The precipitating electron data (solid line) indicates an energy deposition rate of about $20 \text{ erg/cm}^2 \text{ sec}$ in the poleward arc and $10\text{-}15 \text{ erg/cm}^2 \text{ sec}$ within the core, with a low level of precipitation separating the two. Observed characteristic energies were $\sim 15 \text{ keV}$ in the arc, $5\text{-}6 \text{ keV}$ in the gap and near 10 keV in the core. The quantities inferred from the X-ray observations are plotted as crosses, with the horizontal bar indicating the effective spatial resolution of the detector and the vertical bar depicting uncertainties attributable to statistical counting errors in the raw X-ray spectral measurement. The

inferred quantities are, by and large, quite representative of the real world. The ability of the X-ray technique to reproduce the characteristic incident electron energy is particularly notable. The spatial distribution and magnitude of energy flux is also well represented except for a slight underestimate of the energy flux within the poleward arc. This underestimate is probably due to incomplete beam filling of the detector, pointing out the future need for well collimated instrumentation. Note that in Figure 6 the electron and X-ray data have been offset in time by 15 seconds in order to account for magnetic field line tilt between the satellite and the atmosphere.

The second example, shown in Figures 7a, b depicts much quieter auroral conditions, with the energy deposition barely exceeding $1 \text{ erg/cm}^2 \text{ sec}$. Note that the energy flux scale in Figure 7a is one order of magnitude lower than that of Figure 6a. The dusk sector is comprised of a number of detached arcs with energy flux less than $1 \text{ erg/cm}^2 \text{ sec}$ and characteristic energies of about 3 keV. The dawn sector is more spatially continuous with energy deposition of about $1 \text{ erg/cm}^2 \text{ sec}$ at a characteristic energy of about 10 keV. Again, the spectral quantities inferred from the X-ray data are in very good agreement with the observed values, particularly the characteristic energies. The poleward edge of the dawn aurora is underestimated in flux, probably due to decreasing characteristic energy in that region.

These two examples, which represent quite different levels of auroral activity, show that the X-ray technique provides a reasonable representation of the important incident electron spectral parameters, namely integral energy flux, integral number flux and characteristic energy. These parameters are interesting in themselves since the source of plasma in different types of auroral forms is currently a topic of theoretical interest. Imaging X-ray detectors can provide large-scale two-dimensional maps of electron spectral

features within a variety of auroral forms. Further, derived quantities such as the ionospheric conductances can be computed from these same fundamental precipitating electron spectral parameters.

V. Summary

A numerical technique has been developed which provides a statistically optimal estimate of incident auroral electron spectra based on satellite observations of bremsstrahlung X-ray spectra. The technique utilizes a maximum-entropy estimate for the inferred electron spectrum based on discrete observations of the bremsstrahlung spectrum. An integral convolution of the electron distribution by a bremsstrahlung production function is assumed, and measurement errors are incorporated in the model. The measurement errors are constrained in the numerical technique by estimates of the variance due to counting statistics, and a specified confidence level for the χ^2 function. An approximate form of the bremsstrahlung production function is computed in the test; however, the numerical deconvolution scheme does not rely on the particular form derived in this report. The deconvolution scheme therefore can be used as a testbed for other more accurate representations of bremsstrahlung production.

A number of examples are shown which characterize the performance of the numerical model both for ideal cases as well as for actual data. Comparisons between inferred and observed electron spectra show that while current instrumentation suffers from relatively poor signal-to-noise ratio, general characteristics of auroral electron precipitation can be measured remotely by satellite-borne X-ray spectrometers.

References

- Andrews, H. C. and B. R. Hunt, Digital Image Restoration, Prentice-Hall, Englewood Cliffs, New Jersey, 1977.
- Berger, M. J. and S. M. Seltzer, Bremsstrahlung in the atmosphere, J. Atmos. Terr. Phys., 34, 85, 1972.
- Gull, S. F. and G. J. Daniell, Image construction from incomplete or noisy data, Nature, 272, 686, 1978.
- Heitler, W., The Quantum Theory of Radiation, Clarendon Press, Oxford, England, 1954.
- Hubbell, J. H., Survey of photon attenuation coefficient measurements from 10 eV to 100 GeV, Atomic Data, 3, 241, 1971.
- Imhof, W. L., G. H. Nakano, R. G. Johnson and J. B. Reagan, Satellite observations of bremsstrahlung from widespread energetic electron precipitation events, J. Geophys. Res., 79, 565, 1974.
- Imhof, W. L., G. H. Nakano, E. E. Gaines and J. B. Reagan, A coordinated two-satellite study of energetic electron precipitation events, J. Geophys. Res., 80, 3622, 1975a.
- Imhof, W. L., G. H. Nakano and J. B. Reagan, Satellite observations of X-rays associated with energetic electron precipitation near the trapping boundary, J. Geophys. Res., 80, 3639, 1975b.
- Jaynes, E. T., Information theory and statistical mechanics, Phys. Rev., 106, 620, 1957.
- Luhmann, J. G., Auroral electron spectra in the atmosphere, J. Atmos. Terr. Phys., 38, 605, 1976.
- Luhmann, J. G., Auroral bremsstrahlung spectra in the atmosphere, J. Atmos. Terr. Phys., 39, 595, 1977.

- Mizera, P. F., J. G. Luhmann, W. A. Kolasinski and J. B. Blake, Correlated observations of auroral arcs, electrons and X-rays from a DMSP satellite, J. Geophys. Res., 83, 5573, 1978.
- Mizera, P. F., D. J. Gorney and J. L. Roeder, Auroral X-ray images from DMSP-F6, Geophys. Res. Lett., 11, 255, 1984.
- Rees, M. H., Auroral ionization and excitation by incident energetic electrons, Planet. Space Sci., 11, 1209, 1964.
- Wilczek, R. and S. Drapatz, A high accuracy algorithm for maximum entropy image restoration in the case of small data sets, Astron. Astrophys., 142, 9, 1985.

Appendix

The expression relating observable bremsstrahlung flux to volume emissivity, shown below, indicates two angular effects of importance:

$$\Phi(X, \eta) = \int_0^{z_c \sec \eta} dZ \sec \eta P_B(X, Z) \exp(-\mu_a z \sec \eta) \quad (A1)$$

The first effect is purely geometrical, arising from the field-of-view foreshortening at increasing zenith or elevation angle. This effect, along with the concomitant integration over a longer emission column driven by the $\sec \eta$ term, leads to limb brightening. The second effect is increased attenuation due to propagation path lengthening, appearing as the exponential term. This obviously leads to limb darkening. Since the absorption coefficient μ_a is a strong function of X-ray energy, one might expect different trade-offs between limb brightening and limb darkening at different elevation angles and energies. This is indeed the case.

Figure 8 shows a representative profile of atmospheric depth in altitude (Berger and Seltzer, 1972) which we can apply in demonstrating the effects of limb brightening. Figures 9a-d show the ratio of the bremsstrahlung intensity at the top of the atmosphere to that at the source altitude (a parameter) as a function of zenith or elevation angle for several energies covering the auroral range. For X-rays at 20 keV (Figure 9a), limb brightening is apparent for all source altitudes from 90-200 km. The brightening is about a factor of five at 80° elevation angle. Substantial limb brightening is also apparent at $X = 6$ keV, although less brightening occurs for X-rays from the lowest source altitude. Lower energy X-rays, at 2 keV and 1 keV, show significant limb darkening effects for low altitude sources, while maintaining limb brightening for higher source altitudes. The net effect of the limb is an integral over

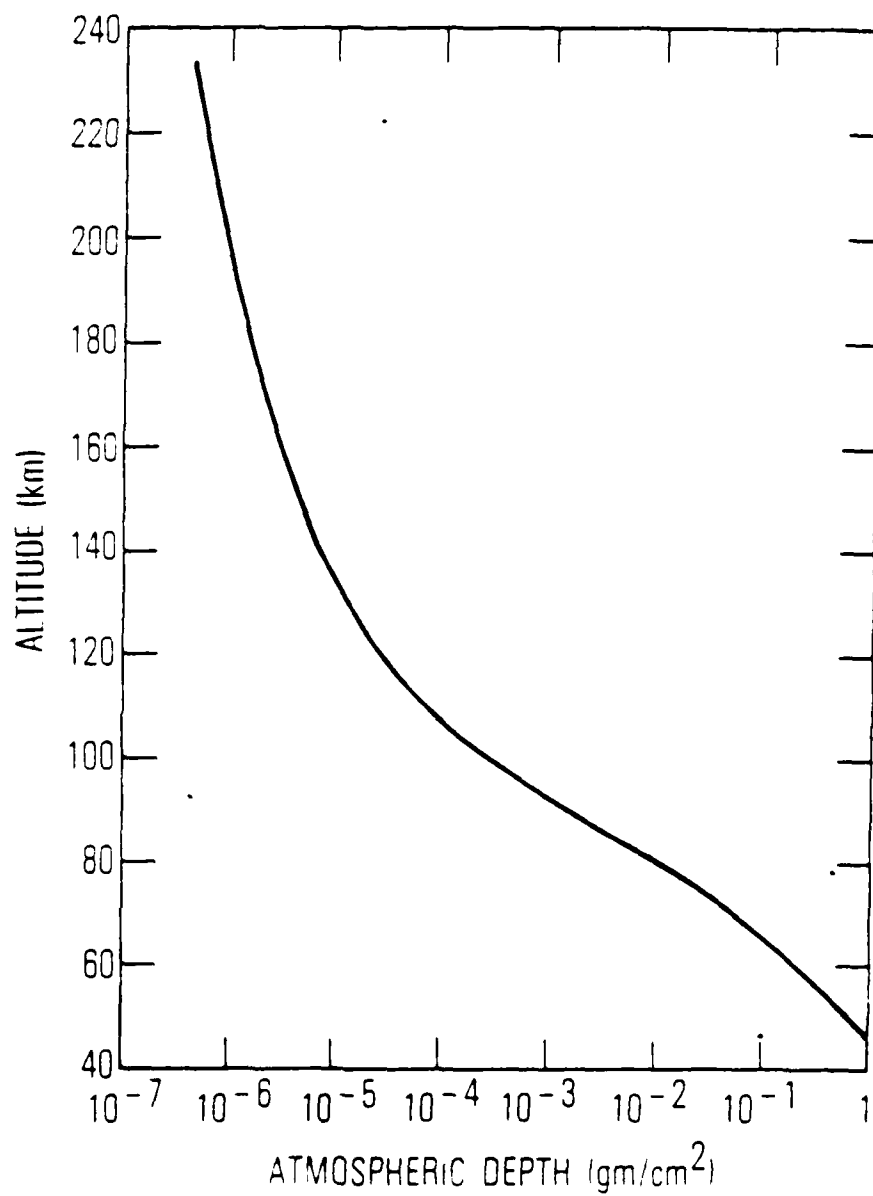


Figure 8. Plot of Atmospheric Depth Versus Altitude (from Berger and Seltzer, 1972)

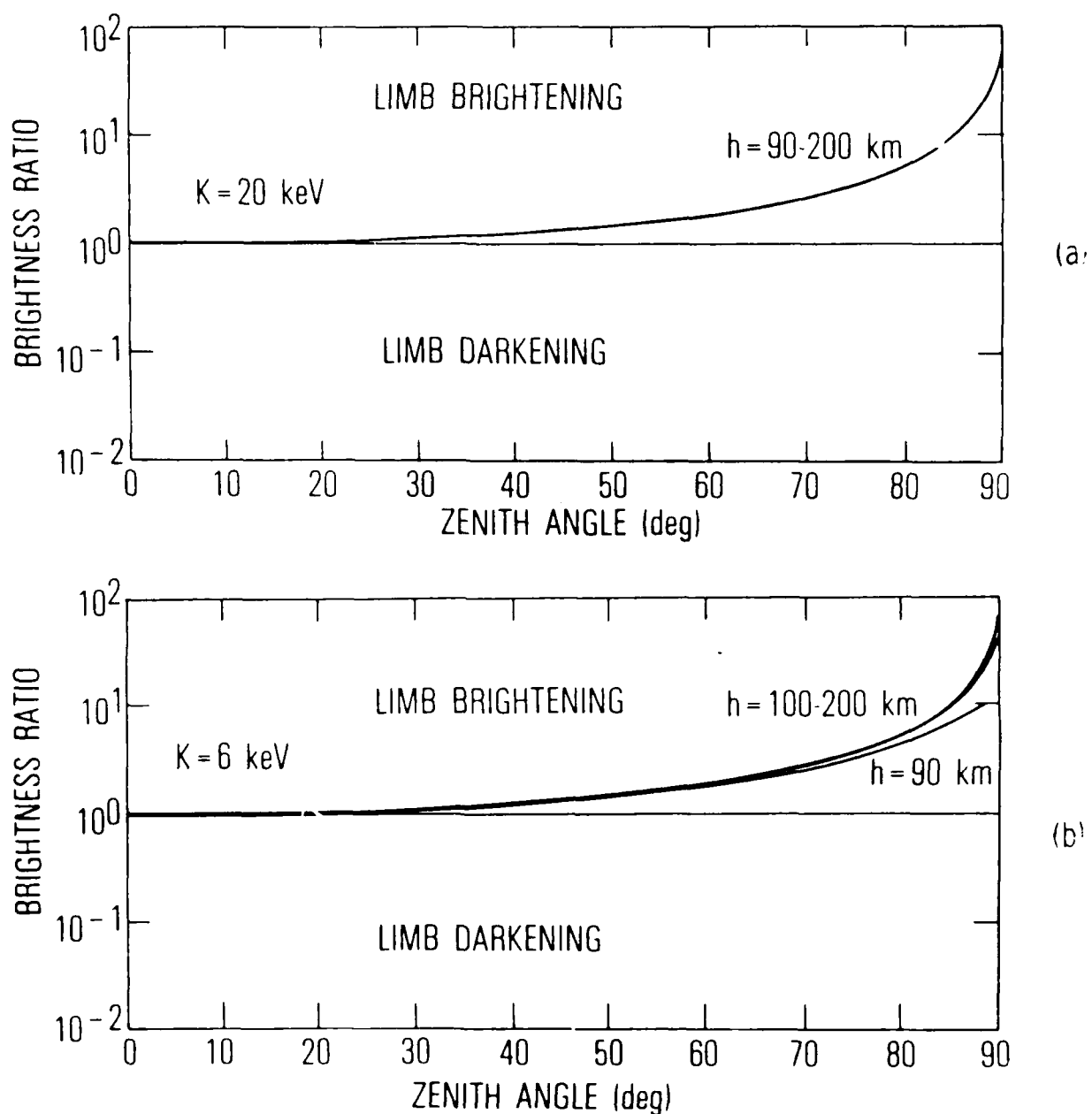


Figure 9a and b. Plots of the Ratio of Bremsstrahlung Intensity at the Top of the Atmosphere To That at the Source Altitude as a Function of Zenith Angle for (a) 20 keV and (b) 6 keV

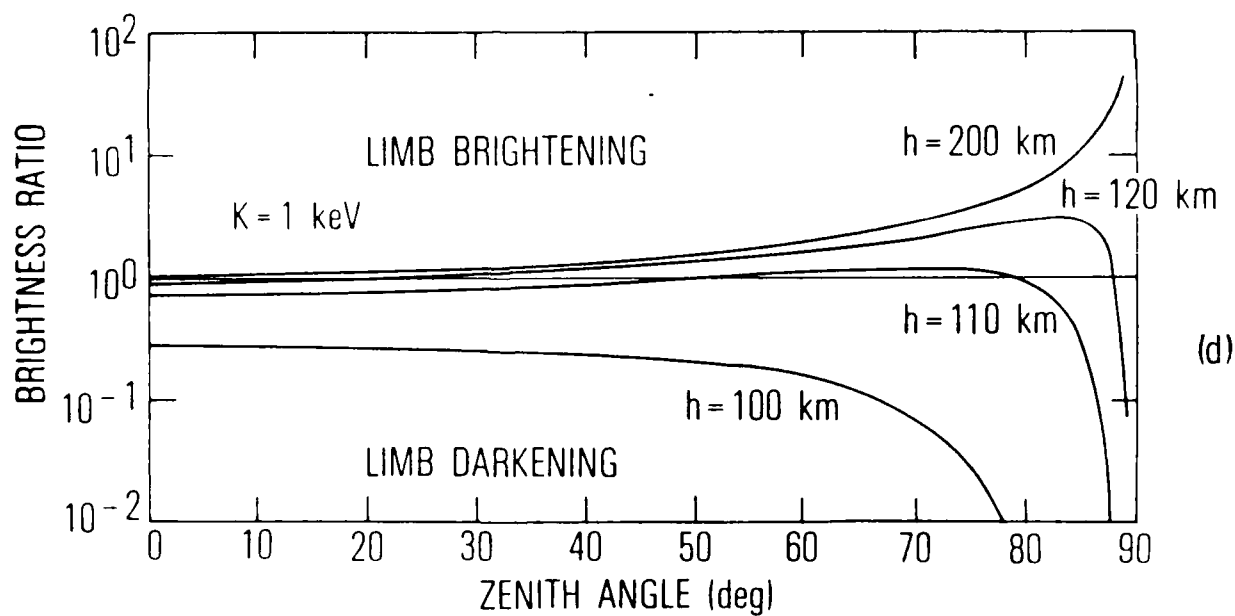
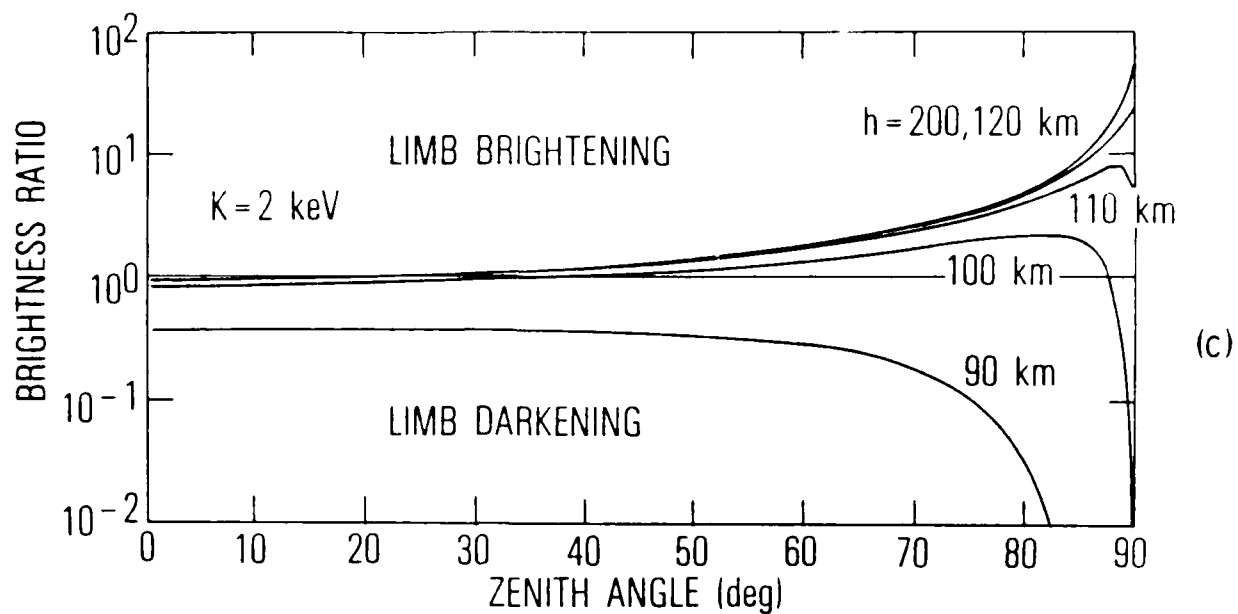


Figure 9c and d. Plots of the Ratio of Bremsstrahlung Intensity at the Top of the Atmosphere To That at the Source Altitude as a Function of Zenith Angle for (c) 2 keV and (d) 1 keV

all source altitudes, which typically results in limb brightening at all energies since low energy X-rays are generally emitted at higher altitudes. Note that the effects of limb brightening or darkening do not become significant until elevation angles exceed about 70° .

LABORATORY OPERATIONS

The Aerospace Corporation functions as an "architect-engineer" for national security projects, specializing in advanced military space systems. Providing research support, the corporation's Laboratory Operations conducts experimental and theoretical investigations that focus on the application of scientific and technical advances to such systems. Vital to the success of these investigations is the technical staff's wide-ranging expertise and its ability to stay current with new developments. This expertise is enhanced by a research program aimed at dealing with the many problems associated with rapidly evolving space systems. Contributing their capabilities to the research effort are these individual laboratories:

Aerophysics Laboratory: Launch vehicle and reentry fluid mechanics, heat transfer and flight dynamics; chemical and electric propulsion, propellant chemistry, chemical dynamics, environmental chemistry, trace detection; spacecraft structural mechanics, contamination, thermal and structural control; high temperature thermomechanics, gas kinetics and radiation; cw and pulsed chemical and excimer laser development including chemical kinetics, spectroscopy, optical resonators, beam control, atmospheric propagation, laser effects and countermeasures.

Chemistry and Physics Laboratory: Atmospheric chemical reactions, atmospheric optics, light scattering, state-specific chemical reactions and radiative signatures of missile plumes, sensor out-of-field-of-view rejection, applied laser spectroscopy, laser chemistry, laser optoelectronics, solar cell physics, battery electrochemistry, space vacuum and radiation effects on materials, lubrication and surface phenomena, thermionic emission, photo-sensitive materials and detectors, atomic frequency standards, and environmental chemistry.

Computer Science Laboratory: Program verification, program translation, performance-sensitive system design, distributed architectures for spaceborne computers, fault-tolerant computer systems, artificial intelligence, micro-electronics applications, communication protocols, and computer security.

Electronics Research Laboratory: Microelectronics, solid-state device physics, compound semiconductors, radiation hardening; electro-optics, quantum electronics, solid-state lasers, optical propagation and communications; microwave semiconductor devices, microwave/millimeter wave measurements, diagnostics and radiometry, microwave/millimeter wave thermionic devices; atomic time and frequency standards; antennas, rf systems, electromagnetic propagation phenomena, space communication systems.

Materials Sciences Laboratory: Development of new materials: metals, alloys, ceramics, polymers and their composites, and new forms of carbon; non-destructive evaluation, component failure analysis and reliability; fracture mechanics and stress corrosion; analysis and evaluation of materials at cryogenic and elevated temperatures as well as in space and enemy-induced environments.

Space Sciences Laboratory: Magnetospheric, auroral and cosmic ray physics, wave-particle interactions, magnetospheric plasma waves; atmospheric and ionospheric physics, density and composition of the upper atmosphere, remote sensing using atmospheric radiation; solar physics, infrared astronomy, infrared signature analysis; effects of solar activity, magnetic storms and nuclear explosions on the earth's atmosphere, ionosphere and magnetosphere; effects of electromagnetic and particulate radiations on space systems; space instrumentation.

END

2-87

DTIC